

RESEARCH ARTICLE

Mars nightside electrons over strong crustal fields

10.1002/2015JA021947

Key Points:

- Electron populations on the nightside of Mars are explored
- Occurrence rates and energy deposition values are calculated
- Median precipitating flux yields a peak n_e of $4.2 \times 10^3 \text{ cm}^{-3}$

Correspondence to:

A. D. Shane,
adshane@umich.edu

Citation:

Shane, A. D., S. Xu, M. W. Liemohn, and D. L. Mitchell (2016), Mars nightside electrons over strong crustal fields, *J. Geophys. Res. Space Physics*, 121, 3808–3823, doi:10.1002/2015JA021947.

Received 22 SEP 2015

Accepted 4 APR 2016

Accepted article online 11 APR 2016

Published online 30 APR 2016

Alexander D. Shane¹, Shaosui Xu^{1,2}, Michael W. Liemohn¹, and David L. Mitchell²¹Department of Climate and Space Sciences and Engineering, University of Michigan, Ann Arbor, Michigan, USA,²Space Sciences Laboratory, University of California, Berkeley, California, USA

Abstract We investigated 7 years worth of data from the electron reflectometer and magnetometer aboard Mars Global Surveyor to quantify the deposition of photoelectron and solar wind electron populations on the nightside of Mars, over the strong crustal field region located in the southern hemisphere. Just under 600,000 observations, each including energy and pitch angle distributions, were examined. For solar zenith angles (SZA) less than 110° , photoelectrons have the highest occurrence rate; beyond that, plasma voids occur most often. In addition, for $\text{SZA} > 110^\circ$, energy deposition of electrons mainly occurs on vertical field lines with median pitch angle averaged energy flux values on the order of $10^7 - 10^8 \text{ eV cm}^{-2} \text{ s}^{-1}$. The fraction of downward flux that is deposited at a given location was typically low (16% or smaller), implying that the majority of precipitated electrons are magnetically reflected or scattered back out. The average energy of the deposited electrons is found to be 20–30 eV, comparable to typical energies of photoelectrons and unaccelerated solar wind electrons. Median electron flux values, from near-vertical magnetic field lines past solar zenith angle of 110° , calculated in this study produced a total electron content of $4.2 \times 10^{14} \text{ m}^{-2}$ and a corresponding peak density of $4.2 \times 10^3 \text{ cm}^{-3}$.

1. Introduction

Unlike the Earth, which has a global magnetic field, Mars has localized crustal magnetic fields [Acuña *et al.*, 1998, 2001]. These crustal fields complicate the interaction with the interplanetary magnetic field (IMF), resulting in a sophisticated magnetic topology [e.g., Mitchell *et al.*, 2001; Nagy *et al.*, 2004; Brain *et al.*, 2007; Liemohn *et al.*, 2007]. The strongest crustal magnetic fields are located in the southern hemisphere [e.g., Connerney *et al.*, 2001]. Brain *et al.* [2007] used electron pitch angle distributions (PADs) from Mars Global Surveyor (MGS) to infer the magnetic field topology of Mars. On the nightside, Brain *et al.* [2007] classified two-sided loss cones (trapped populations) and plasma voids (locations where the observations are at or near the instrument background level), as indicators of closed magnetic field lines corresponding to the Martian crustal fields. In contrast, nightside one-sided loss cones often are related to open/draped field lines, suggesting connection to the IMF, allowing planetward streaming electrons on one end and atmospheric absorption on the other. In particular, radial crustal fields form magnetic cusps generally located between magnetic loop structures. These cusps are ideal locations for solar wind/magnetosheath electrons to precipitate [Mitchell *et al.*, 2001; Liemohn *et al.*, 2003; Safaenili *et al.*, 2007; Xu *et al.*, 2014b]. Němec *et al.* [2010] found that the occurrence rate of nightside ionosphere patches observed by Mars Express is 4 times larger over cusp regions rather than where the magnetic field is horizontal.

Day-to-night plasma transport and electron precipitation are both important mechanisms for the creation of the nightside ionosphere of Mars [e.g., Fox *et al.*, 1993]. Verigin *et al.* [1991] used an analysis of the hyperbolic electrostatic analyzer (HARP) measurements from PHOBOS 2 to propose that a characteristic omnidirectional electron flux of $\sim 10^8 \text{ cm}^{-2} \text{ s}^{-1}$ is sufficient to create the nightside ionosphere. Haider *et al.* [1992] confirmed this to be true given that the electrons are precipitating. Liemohn *et al.* [2007] showed that some closed field lines straddle the terminator, allowing photoelectrons to precipitate into the nightside ionosphere. The nightside precipitation variability due to solar wind was investigated by Lillis and Brain [2013] and found that plasma voids vary significantly with solar wind pressure.

Haider *et al.* [2007] calculated that solar wind electron precipitation creates a peak ion layer at $\sim 130 \text{ km}$. Němec *et al.* [2011] observed enhanced ionization over magnetic cusp regions. This localized ionization, especially when enhanced, can cause density gradients up to $600 \text{ cm}^{-3} \text{ km}^{-1}$ [Fillingim *et al.*, 2010]. They found that

density gradients can lead to plasma transport resulting in currents and Joule heating. *Němec et al.* [2010] concluded that most of the nightside ionosphere has a peak electron density lower than $5 \times 10^3 \text{ cm}^{-3}$ and that over strong crustal field regions, the peak density does not vary with solar zenith angle (SZA), implying that electron precipitation is the main mechanism for the formation of nightside ionosphere over such regions.

Excitation, the cause for aurora on the nightside, is another consequence of precipitating electrons. Here on Earth there are primarily two types of aurora, diffuse and discrete; a review of terrestrial aurora can be viewed in *Swift* [1981]. The diffuse aurora is caused by scattering of electrons in the plasma sheet into the loss cone that precipitate into our atmosphere [e.g., *Ashour-Abdalla and Kennel*, 1978]. Field-aligned acceleration mechanisms are the primary cause for the discrete aurora. Characteristic energy of precipitating electrons on Earth is $\sim 2\text{--}3 \text{ keV}$, but auroral electrons can range from 0.5 to 40 keV. Aurora on Venus are thought to be produced by electrons with energies less than 300 eV [*Fox and Stewart*, 1991]. The first reports of aurora emission on Mars came from the ultraviolet spectrometer (Spectroscopy for Investigation of Characteristics of the Atmosphere of Mars, SPICAM) on board Mars Express (MEX) [*Bertaux et al.*, 2005]. They reported aurora different from any other seen in our solar system. The Martian aurora reported was controlled by the crustal fields and was localized and highly concentrated. *Leblanc et al.* [2008] found a strong connection between auroral events and magnetic cusps. Several others have investigated auroral electron spectra from MGS [e.g., *Brain et al.*, 2006] and Mars Express [e.g., *Lundin et al.*, 2006a, 2006b]. *Leblanc et al.* [2006] and *Dubin et al.* [2008a] proposed that the auroral electron energy distribution seen by Mars Express peaked at a few tens of eV. The accelerated electrons in these papers have enough energy to produce auroral emissions. Recently, *Soret et al.* [2015] used a Monte Carlo model to find that the height of observed auroral emission from SPICAM could be recreated with electrons between 50 and 1000 eV. *Gérard et al.* [2015] did not find a correlation between the observed UV aurora and downward electron flux measurements at the Mars Express altitude. This could be due to the fact that the field lines where the aurora is occurring are not vertical but tilted so the spacecraft is not measuring them. Another possibility is an acceleration process occurring below the spacecraft.

Brain et al. [2005] investigated magnetosheath plasma intrusions below 400 km on the dayside and analyzed its dependence on IMF orientation and on seasons. They found that crustal magnetic fields raise the magnetic pileup boundary and that cusps allow sheath electrons to enter the atmosphere. *Brain et al.* [2007] also examined the dayside magnetic field structure using PAD. They recorded isotropic distributions near strong crustal field regions. A new method of separating photoelectrons from solar wind electrons (classifying by energy spectra rather than PAD) was used by *Xu et al.* [2014b] in their statistical study of dayside solar wind precipitation on the magnetic cusps. They investigated the occurrence rates of both populations and dependence on solar zenith angle, magnetic elevation angle, and seasonal variation. They compared the solar wind energy deposition to solar EUV flux input and found that it was 0.1%–2% of the solar EUV flux.

This study is concerned with the nightside (SZA $>90^\circ$) of Mars and will use the same population classification method used by *Xu et al.* [2014b]. The net energy deposition of electrons over the strong crustal field region will be investigated, something which has not been calculated yet on the nightside, as a function of solar zenith angle and magnetic elevation angle. The fractional deposition rate and the average energy of deposited particles will be analyzed. Finally, the consequences of electron deposition, i.e., excitation and ionization, will be examined.

2. Methodology

The electron reflectometer (ER) on board MGS recorded superthermal electron angular distributions ranging from energies of 10 eV to 20 keV. The field of view spanned $360^\circ \times 14^\circ$ and was divided into sixteen 22.5° sectors. Measurements from sectors 8, 10, and 11 were discarded due to high fluxes being recorded frequently, regardless of field line orientations [*Xu et al.*, 2014a]. With the magnetic field information from the magnetometer (MAG), these angular distributions can be converted into PADs [*Mitchell et al.*, 2001]. Important to note is the uneven sampling by the ER due to the orientation of the magnetic field with respect to the ER. If the magnetic field was perpendicular to the plane of the field of view, field-aligned pitch angles were not sampled [see *Liemohn et al.*, 2006, Figure 9]. If the magnetic field was parallel to the plane, then the entire PAD was sampled. “Modified pitch angles” were used similar to *Xu et al.* [2014b] to identify if the electrons were moving toward or away from the planet. If the magnetic field is positive (directed away from the planet), then the pitch angles were flipped, for example, pitch angles of 10° become pitch angles of 170° . In the end, pitch

angles are organized into 10° bins with 0°–90° directed toward the planet (i.e., downward) and 90°–180° directed away from the planet (upward). From this point forward in the text, all pitch angles are modified.

MGS orbit was locked to 0200/1400 local time at an altitude of 405 ± 36 km. All measurements with a solar zenith angle of less than 90° were excluded to limit this study to the nightside. *Xu et al.* [2014a, 2014b] conducted the analogous studies for the dayside strong crustal field regions. Another stipulation added was to focus this study on the strong crustal fields located in the southern hemisphere, as the magnetic cusps in this region are more likely to allow electron precipitation to enter the thermosphere below 200 km and cause enhanced ionization and excitation. The data were filtered to only include data within a box spanning from 160° to 200° east longitude and 30° to 70° south latitude. To make sure that the crustal fields and not piled up IMF were being measured, *Xu et al.* [2014b] used a minimum magnetic field strength of 35 nT in their dayside study. On the night side, the IMF does not build up; therefore, the minimum magnetic field strength used is 5 nT (removal of 74 observations), to ensure pitch angle accuracy. It is still possible, however, that noncrustal field lines are included in the remaining observations. Overall, this yielded ~600,000 observations over 7 years of collected data, each with pitch angle and energy distributions.

Many energy spectra had values under the background flux levels or resembled the background curve. The nightside does not have a constant plasma source term; therefore, plasma voids are common. Plasma voids occur on closed magnetic field lines that have lost their photoelectron population and are isolated from solar wind plasma [*Mitchell et al.*, 2001]. Two conditions were used on each energy spectrum to filter out voids. The 190, 115, 79, 61, 47, and 36 eV energy channels were chosen, and if more than one of these flux values fell below the background level, then it was classified as a void (Figure 1a). If the flux is close to the background, the signal-to-noise ratio of the measurement is low, making the observation unreliable. Even if they are distinguishable from the background, the fluxes will be too low to cause significant impact to the Martian nightside ionosphere/thermosphere. However, many spectra existed that have the same shape as the background curve similar to Figure 1b. The “cliff” in the background curve is from a change in the instrument geometry factor at higher energies. This type of spectra does not meet our above criteria but is also suggestive of a void. To filter such observations out, the same six energy channels were chosen and the measured flux was divided by the background flux and the standard deviation was computed. These same six flux channels envelop the background cliff. If the ratio of background flux to measured flux is similar in all six channels, this means that the measured flux as a curve is close to the background. Therefore, if the standard deviation of these six ratios is small, we know that all the channels have similar ratios. If the standard deviation was below 2, indicating a rather “flat” distribution mimicking the background values, then the spectrum was also considered a void.

An important value is the solar zenith angle which divides sunlit areas from darkness or the terminator. Photoelectrons measured by MGS transport from the main source regions at 100–200 km to 400 km along closed magnetic field lines. While the production peak of photoelectrons is roughly located around 130 km, these electrons mostly lose energy locally due to collisions with the neutral atmosphere. Only above a certain altitude, or supposed “superthermal electron exobase,” can photoelectrons transport to high altitudes [*Nagy and Banks*, 1970]. This superthermal electron exobase varies from an altitude of 140 km to 180 km, as reported by several studies [e.g., *Mantas and Hanson*, 1979; *Lillis et al.*, 2008; *Steckiewicz et al.*, 2015; *Xu et al.*, 2016a, 2016b]. To ensure no source, we used an altitude of 200 km to calculate this photoelectron source terminator. A base altitude of 90 km was chosen instead of the surface of Mars as we are assuming that the light will be attenuated by the atmosphere below this altitude. The terminator was computed to be $\text{SZA} \approx 104^\circ$ at an altitude of 200 km. Beyond this solar zenith angle, it is considered that there is no source term for photoelectrons.

The modified pitch angle approach allowed us to take the absolute value of the magnetic elevation angle data. Doing so shrinks the range from the usual -90° to $+90^\circ$ to a reduced range of just 0° – 90° . Elevation angles with values of 0° are tangential with respect to the planet, and angles with values of 90° are radial with respect to the planet.

3. Results

3.1. Determination of Populations

Xu et al. [2014b] used the electron flux ratio of multiple energy pairs (26 eV/115 eV, 36 eV/115 eV, and 47 eV/115 eV) to identify the populations of photoelectrons and solar wind electrons. Photoelectrons have a characteristic “knee” in their spectra near 60–70 eV (due to a drop of solar photons below 15 nm), while solar wind (magnetosheath) electrons do not (Figure 1c). Therefore, taking the flux of an energy channel above

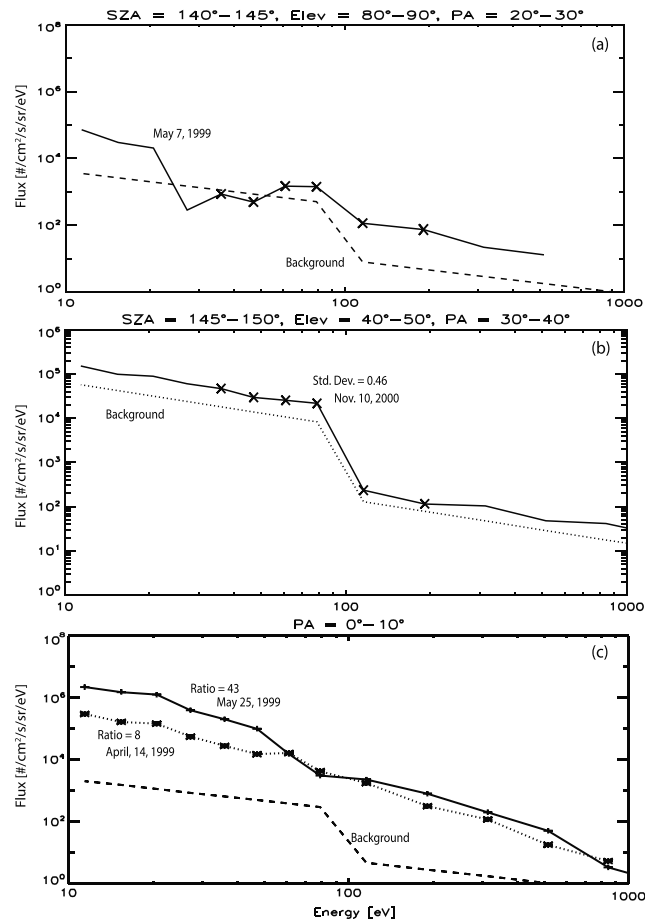


Figure 1. These are three different plots of energy spectra at different times, pitch angle, solar zenith angle, and elevation angle. Pitch angles are modified. (a) An example matching our first criteria for a void-like spectrum. (b) An example matching our second criteria for a void-like spectrum. (c) The solid line is at $SZA = 90^\circ$ and $B_{elev} = 24^\circ$ with a flux ratio of 43, denoting photoelectrons. The dotted line is at $SZA = 145^\circ$ and $B_{elev} = 85^\circ$ with a flux ratio of 8, denoting solar wind electrons.

and below the knee will give a larger ratio for photoelectrons than solar wind electrons. For the flux ratio of 47 eV/115 eV, the population of solar wind electrons had an upper bound of 14 and the photoelectrons had a lower bound of 19 in Xu et al. [2014b]. In this study, a flux ratio of 16 will be used as a hard cutoff in which samples with a ratio above 16 are considered photoelectrons and below as solar wind electrons. Doing so allows us to classify all observations as photoelectron, solar wind electron, or void.

Histograms of the flux ratio as a function of solar zenith angle are shown in Figure 2. All histograms are at pitch angles of $90^\circ - 100^\circ$, because this pitch angle range has the most points due to the instrument field of view limitation. These histograms show either one or two population distributions. As shown in Figure 2a, the histogram has a one-population distribution with a peak ratio ~ 28 suggesting photoelectrons dominating for $SZA = 90^\circ - 105^\circ$. It is expected since the atmosphere is still sunlit, even though $SZA > 90^\circ$. As the solar zenith angle increases, the distribution becomes bimodal with another peak at ~ 7 (Figure 2b), suggesting access of both photoelectrons and solar wind electrons to this location. Abruptly at the $110^\circ - 115^\circ$ solar zenith angle bin, the histograms revert back into a single-population distribution, as the photoelectron peak decays, with peak ratio ~ 5 , indicative of a solar wind population (Figure 2c).

To analyze the dependence on magnetic elevation angle, we divided the data set into three solar zenith angle ranges, $90^\circ - 105^\circ$, $105^\circ - 130^\circ$, and $130^\circ - 155^\circ$. Figure 3 displays histograms of these three ranges split into multiple magnetic elevation angle bins. Again, all histograms are at pitch angles of $90^\circ - 100^\circ$. Note that the y axis is not constant across the plots. Figures 3a–3c show that the relative size of the solar wind electron population to the photoelectron population increases with increasing magnetic elevation angle. Solar wind

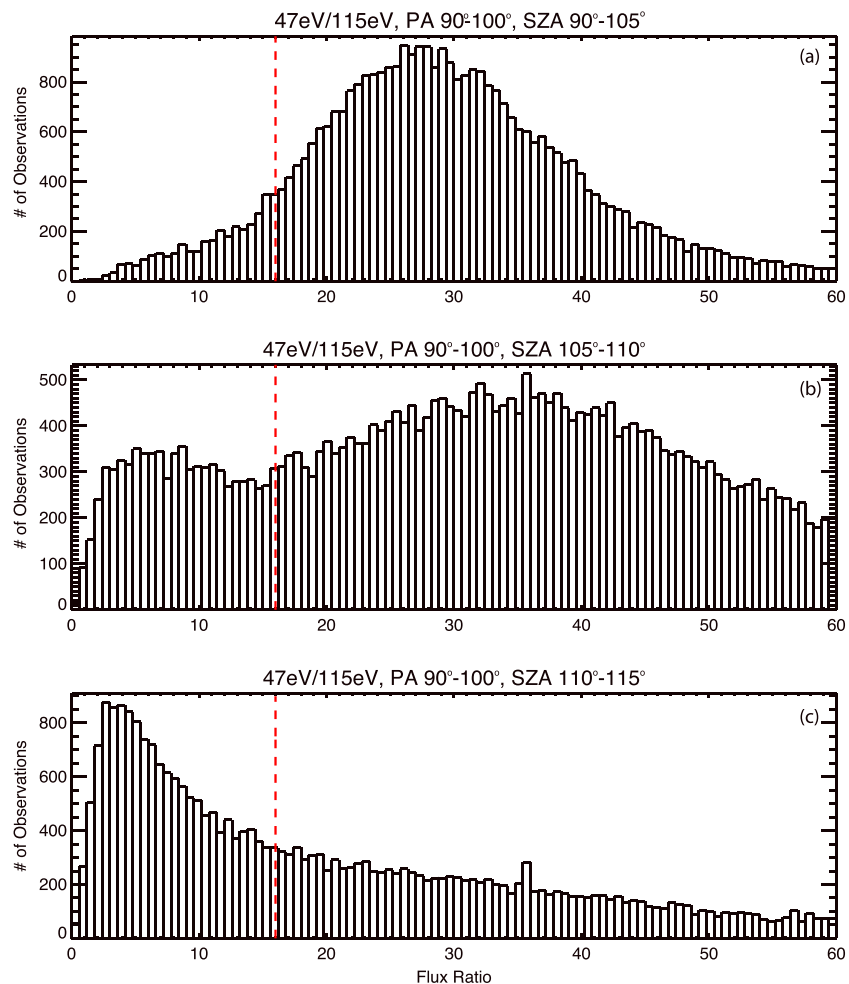


Figure 2. Histograms of the flux ratio (47 eV/115 eV) for modified pitch angles of 90°–100° and (a) SZA = 90°–95°, (b) SZA = 105°–110°, and (c) SZA = 110°–115°. A red dashed line marks the flux ratio, 16, in which samples above are considered photoelectrons and samples below as solar wind electrons.

electrons enter through crustal field lines connected to the IMF, and at 400 km altitude over the strong crustal field regions, these field lines are more likely to be vertical. Figures 3d–3f show that the relative size of the photoelectron population to the solar wind electron population decreases with elevation angle. Photoelectrons at these solar zenith angles are more likely to be trapped on closed field lines. Figures 3g–3i reiterate that a photoelectron population does not exist at high solar zenith angles. The sample number of each population, however, cannot be directly compared, because MGS measured each elevation angle bin unevenly for a given solar zenith angle due to the seasonal effect. Thus, we determine the occurrence rate of each electron population by normalizing the sample number by the total observations in each bin.

3.2. Occurrence Rate of Electron Populations

Every measurement can be labeled as void, photoelectron, or solar wind electron. Figure 4 shows the occurrence rates of the three classifications against pitch angle and solar zenith angle. The occurrence rate is the fraction of data points in that bin with that particular classification. Each bin has at least 1000 data points with the average being around 32,000 data points. Voids are most prevalent once the spacecraft is past the photoelectron source terminator and for field-aligned pitch angles (in the loss cone). Diagrams of this loss cone can be seen in Figure 3 of *Liemohn et al. [1997]*. Electrons with downward field-aligned pitch angles, i.e., near 0°, are more likely to make it farther into the ionosphere and be lost, and since this study is solely on

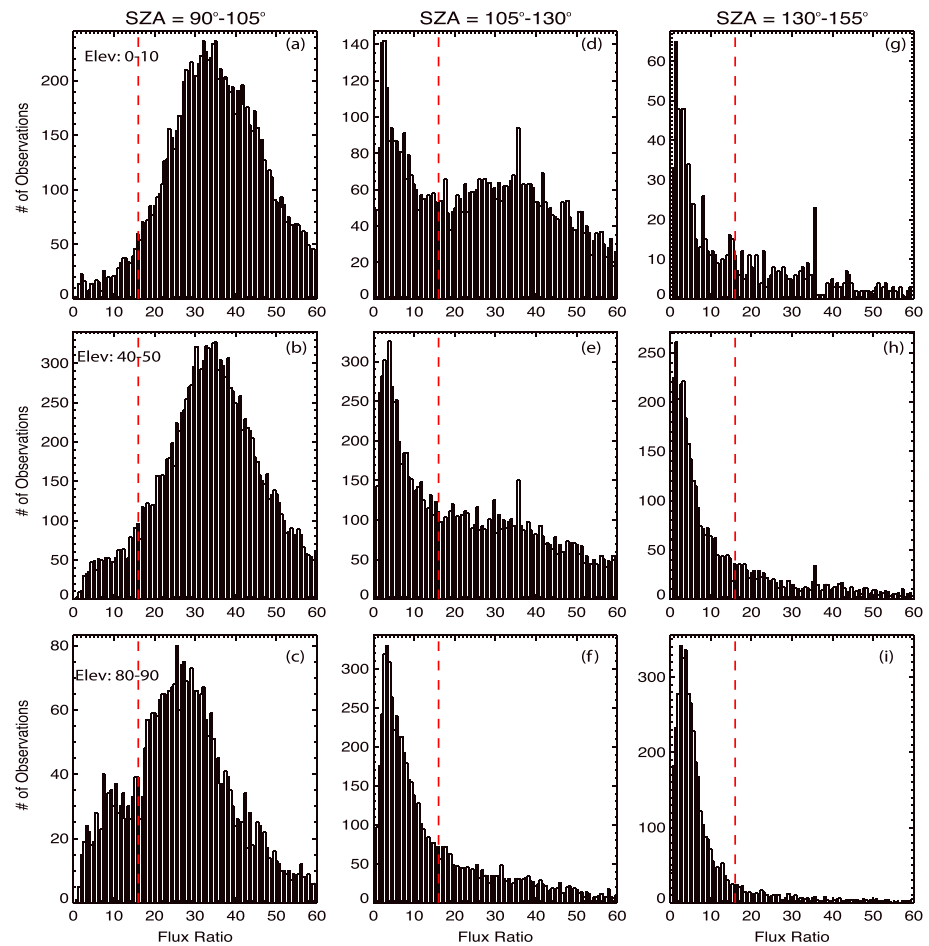


Figure 3. The columns are for different solar zenith angle ranges, from left to right: (a–c) 90° – 105° , (d–f) 105° – 130° , and (g–i) 130° – 155° . The rows are for different magnetic elevation angle ranges of 0° – 10° , 40° – 50° , and 80° – 90° , from top to bottom. All histograms are sampled from modified pitch angles 90° – 100° . A red dashed line marks the flux ratio, 16, in which samples above are considered photoelectrons and samples below as solar wind electrons.

the nightside, there are not many electrons escaping with upward directed pitch angles, i.e., near 180° . Electrons with perpendicular pitch angles will mirror at higher altitudes, being less exposed to the denser ionosphere at lower altitudes. Photoelectrons populate sunlit areas, but once past the terminator, the population decays due to lack of a source term. The photoelectron’s energy degrades, and the electron becomes part of the thermal population, which has low enough energy to recombine. Solar wind electrons have an increase in their occurrence rate past the terminator and remain relatively constant throughout the nightside.

More insight can be gained by plotting the occurrence rate as a function of pitch angle and elevation angle for a range of solar zenith angles. In Figure 5, the occurrence rate is plotted for both photoelectrons and solar wind electrons to see their behavior with increasing solar zenith angle. The average sample size is 3000 data points but never drops below 300. Photoelectrons are completely dominant for solar zenith angles of 96° – 99° (Figure 5a), which is still magnetically connected to a sunlit source region. As solar zenith angle increases, the occurrence rate of photoelectrons decreases from Figures 5a to 5b, as the source weakens while crossing the photoelectron source terminator. In contrast, the photoelectrons at perpendicular pitch angles are trapped populations, bouncing at high altitudes where collision frequency is much lower. The occurrence rate becomes lower at small elevation angles, i.e., more horizontal magnetic fields, from Figures 5b to 5c and on to 5d. At the altitude of MGS, shorter loop structures tend to be horizontal, thus easier for photoelectron energies to degrade due to more frequent collisions with neutral particles, compared to more vertical/taller magnetic field structures. The solar wind population occupies vertical field lines that are more easily connected to the IMF. The solar wind occurrence rate eventually becomes constant once the photoelectron population has sufficiently degraded below the instrument detection threshold as shown in Figures 5i and 5j.

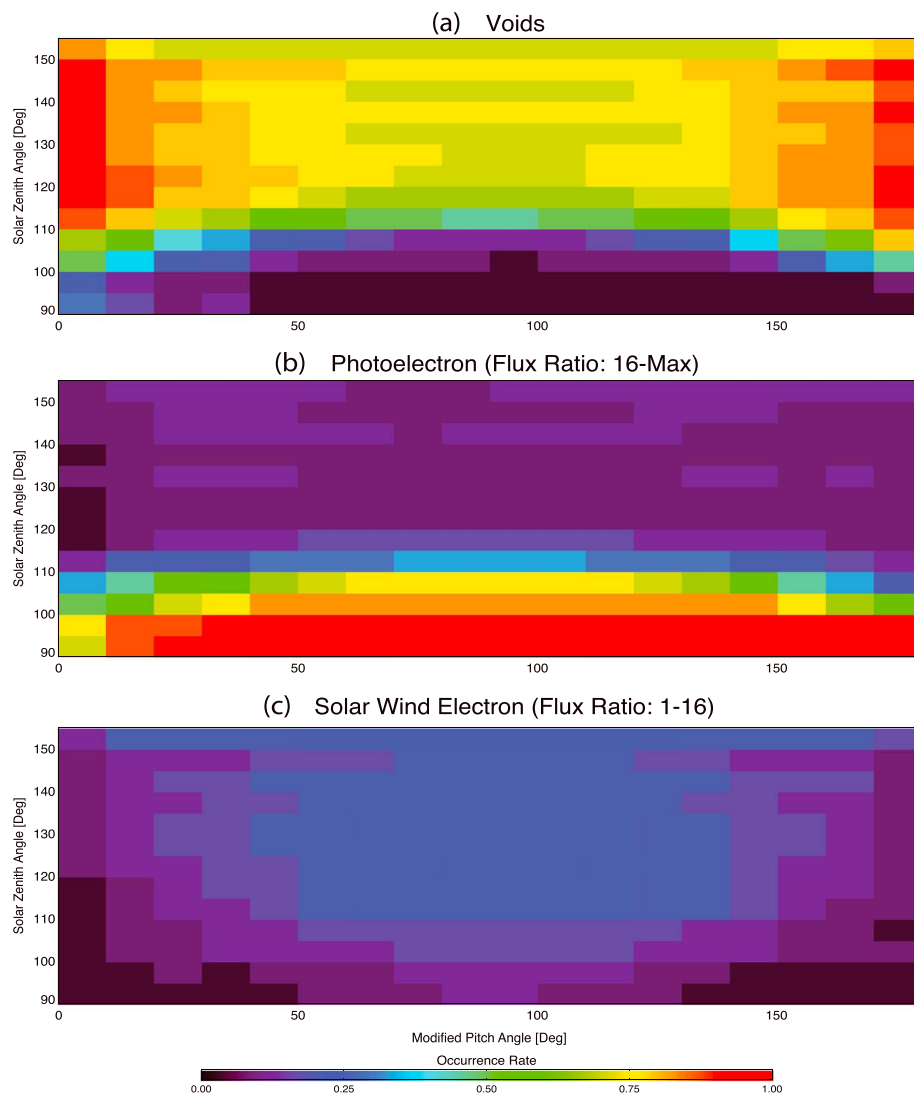


Figure 4. Occurrence rates for (a) voids, (b) photoelectrons, and (c) solar wind electrons as functions of solar zenith angle and modified pitch angle.

At $SZA = 117^\circ - 120^\circ$ (Figures 5e and 5j), the photoelectron population is a “shadow” of the solar wind population, same shape but small fraction of the values. Figure 3h is indicative of a solar wind population, yet the measurements in the tail of the distribution are being classified as photoelectrons. This shadow is an artifact of our classifying method, and the photoelectrons have degraded by this point.

3.3. Energy Deposition

The energy deposition due to superthermal electrons precipitating into the Martian ionosphere is important for ionization, local heating, and excitation (aurora on the nightside and dayglow on the dayside). Figure 6 displays the calculated median pitch angle averaged upward, downward, and net deposited (downward-upward) energy fluxes by elevation angle and solar zenith angle. The deposited flux is not a subtraction of the two medians, but first, the deposited flux was calculated for each observation and then the median is found. This calculation was done with voids and without voids, the first and second columns, respectively. Furthermore, the energy fluxes are integrals across the entire ER energy range from ~ 10 eV to ~ 20 keV, not just the six energy channels used to classify voids in the earlier section. Sample sizes for Figures 6a–6c have an average of 6000, while the average sample size for Figures 6d–6f is 4000 and neither drop below 100. For Figure 6d, only measurements with voids across all upward pitch angle bins were discarded and the same for Figure 6e with downward bins. Figure 6f had measurements discarded only if all 18 pitch angle bins were classified as voids. Gray boxes have negative values on the order of $10^6 - 10^7$ eV/cm²/s,

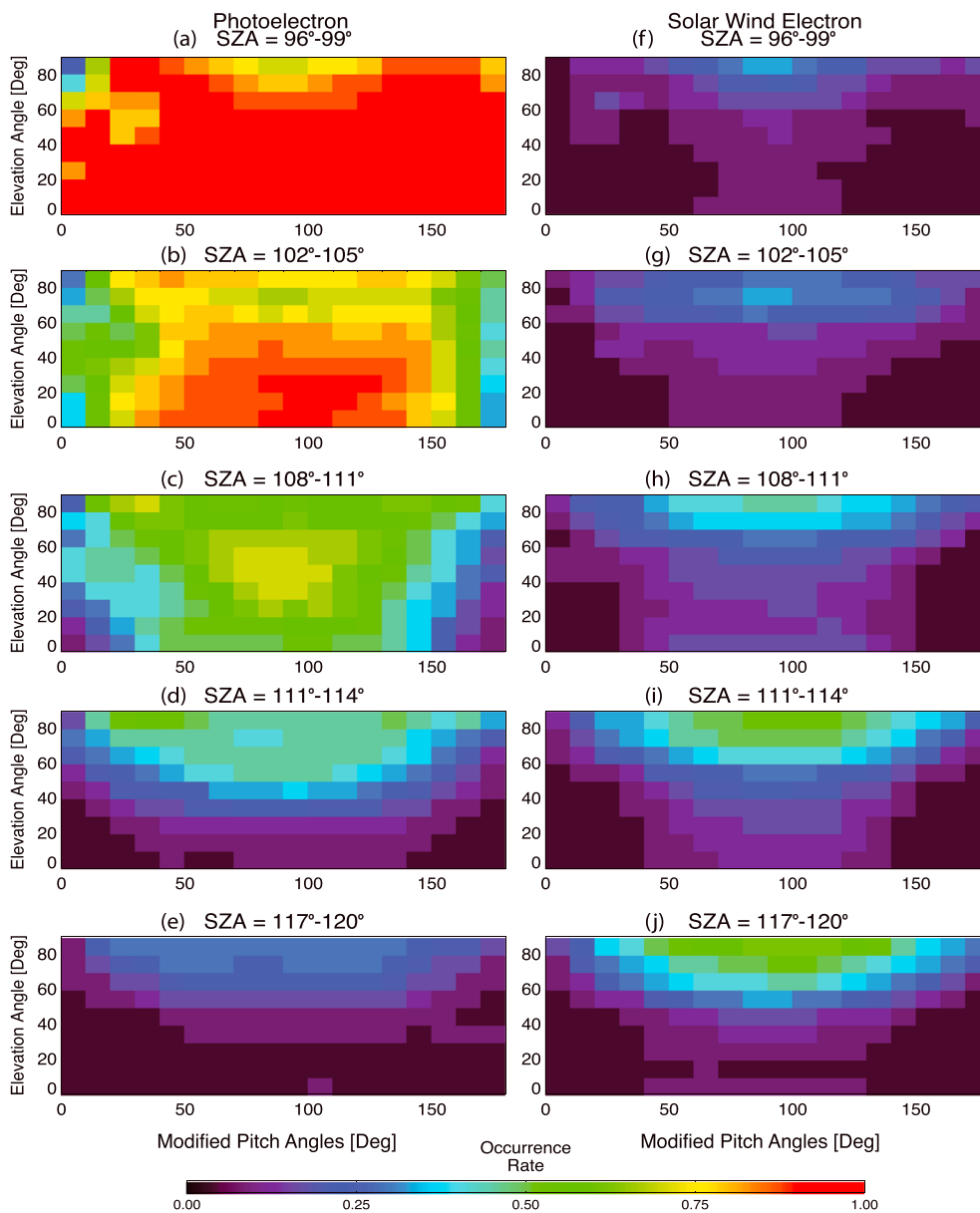


Figure 5. Occurrence rates for (a–e) photoelectrons and (f–j) solar wind electrons. The rows are for solar zenith angles 96°–99°, 102°–105°, 108°–111°, 111°–114°, and 117°–120° (top to bottom).

while a few get as low as 10^4 or as high as 10^8 , indicating a net upward flow. The black boxes in Figures 6a–6c have median values of 0 eV/cm²/s; i.e., the median is within the void population of spectra classifications. For comparison, 6.2×10^{11} eV/cm²/s is equivalent to 1.0 mW/m².

From these plots we can identify two regions, one where the amount of voids is significant enough to obscure calculations and another where they are not. The void populated region in Figure 6c, i.e., where the deposited flux is zero, now contains net upward fluxes when the voids are removed (Figure 6f). Histograms of the net energy flux in this region show a bimodal distribution with two peaks on either side of zero for Figure 6f. These regions in both Figures 6d and 6e are so similar that the subtraction between the two appears to be zero. Also, the pitch angle averaged energy spectra for both the upward and downward directions in this region are very close to each other, probably within measurement error. The median is probably not a good value to represent this type of distribution (bimodal) found in the gray bins, and the upward net flux is likely to be noise. The inclusion of voids gives us an idea of what we might observe with any random measurement constrained

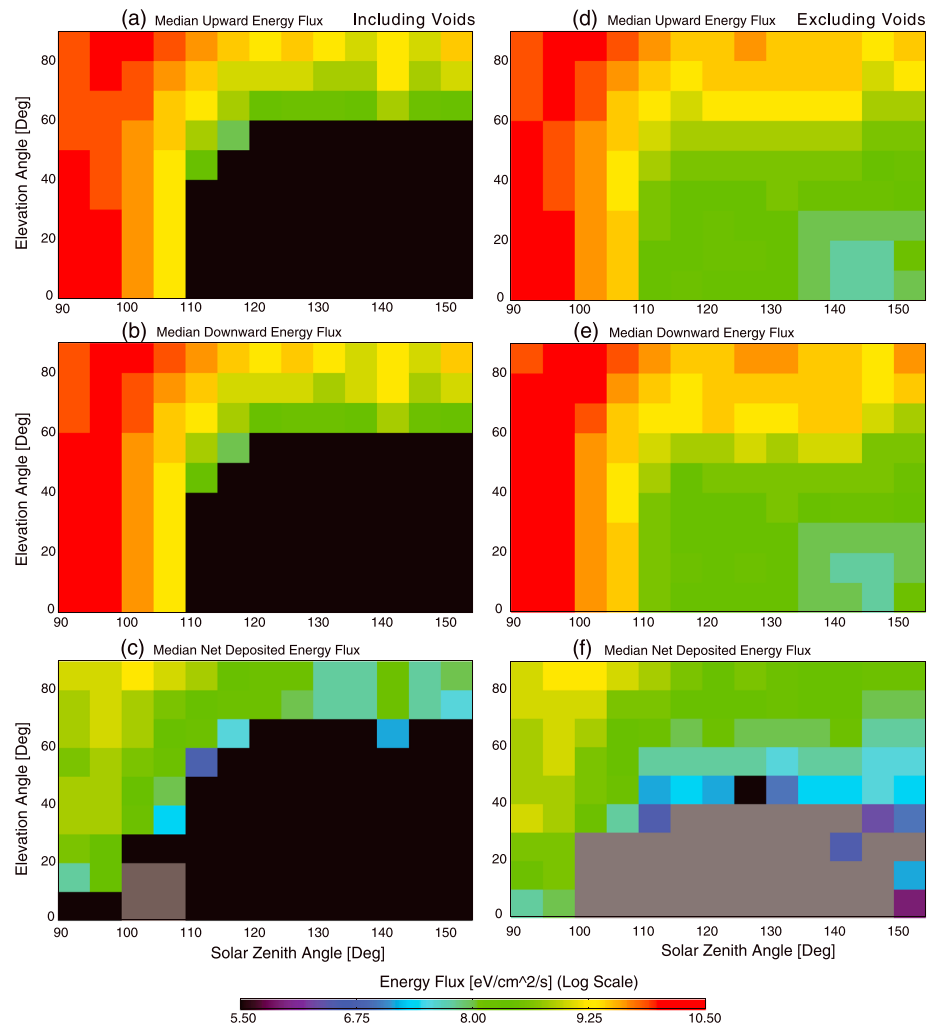


Figure 6. Median pitch angle averaged energy fluxes for (a, d) upward directed electrons, (b, e) downward directed electrons, and the (c, f) net deposited (downward-upward) energy flux. Figures 6a–6c include voids in the calculations, and Figures 6d–6f do not. Gray boxes have negative values on the order of 10^6 – 10^7 eV/cm²/s, while a few get as low as 10^4 and as high as 10^8 .

to the orbit of MGS. What we might observe when electrons are precipitating is given in Figures 6d–6f, i.e., where we have excluded voids.

Energy deposition past SZA=110° is due to solar wind electrons. Figures 2 and 4b show the disappearance of the photoelectron population at this solar zenith angle. Typical postphotoelectron source terminator pitch angle averaged deposited flux values occur primarily on near-vertical field lines with an average value of 2.0×10^8 eV/cm²/s.

Not all downward flux will be deposited into the ionosphere to cause ionization, heating, and excitation. The fractional deposition rate is calculated by dividing the net deposited flux by the downward flux. It is unitless and is the percentage of downward flux that is deposited. Voids have been excluded in this calculation. Figure 7 shows the median value for each solar zenith angle, elevation angle bin. Gray boxes have negative values with magnitude ~ 0.001 – 0.05 , suggesting that these negative values are indeed noise. The fractional deposition rate provides insight as to where there is a higher rate of magnetic reflection and/or backscattering. The rate is low for the first solar zenith angle bin, 90°–95°, where the flux tube is fully sunlit and the upward and downward fluxes are very similar. As we move to higher solar zenith angles, the locally generated (i.e., upward) fluxes are reduced and therefore there is a greater net downward flux. Once past SZA=110°, where the photoelectrons have vanished, the deposition rate decreases due to the lack of a magnetic

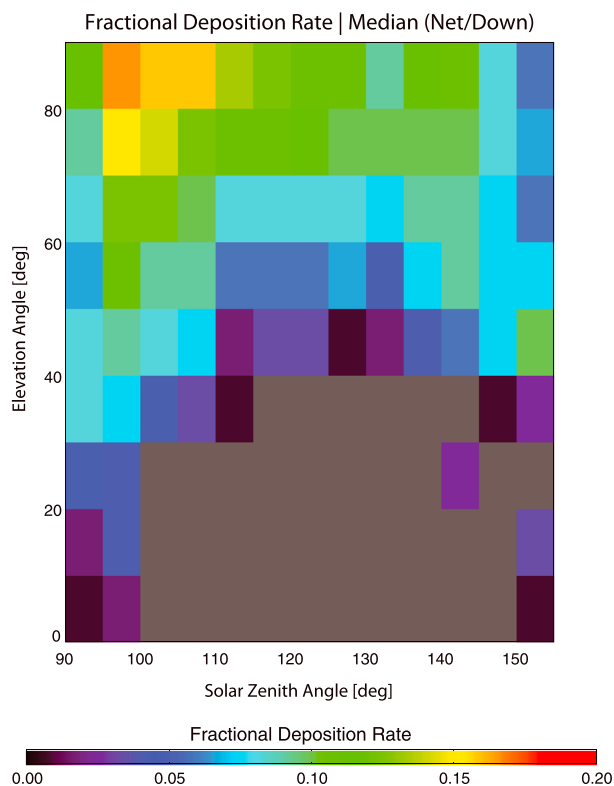


Figure 7. The median of the fractional deposition rate (net flux divided by downward flux), which is the fraction of downward flux that is deposited. Voids are excluded in this calculation. Gray boxes have negative values with magnitudes around $\sim 0.001-0.05$.

footprint in the sunlit ionosphere, restricting electron transport into the nightside. The rate is fairly constant on the nightside, due to only solar wind electrons precipitating. The decrease in neutral density from day to night (about a factor of 3 [Keating *et al.*, 2007]) could also be a reason for the decrease in deposition rate with solar zenith angle. A decrease in neutral density will lower the frequency of collisions, allowing more electrons to be reflected/backscattered before depositing their energy. Vertical field lines correspond to longer field structures; therefore, the electron travels a longer path and has more opportunities to deposit its energy. The highest median fractional deposition rate is 0.16 meaning 84% of the downward flux is reflected/scattered out. Each bin had at least one instance where the deposition rate was at least 0.85. There are times where the majority of electrons are deposited, across all solar zenith angles and elevation angles, but it does not happen often.

3.4. Average Energy

The energy of an average electron is an important calculation due to implications involving the ionization of neutrals and the depth it will cause ionization at [Banks *et al.*, 1974]. The average energy of an electron was calculated, and the median is plotted against solar zenith angle and elevation angle in Figure 8. The average energy was calculated by dividing the energy flux by the number flux, both integrated over energy and pitch angle. Figure 8 shows upward directed electrons, downward directed electrons, and deposited electrons, from top to bottom, respectively. In order to calculate the upward average energy, only the upward pitch angle bins for the number and energy fluxes are integrated over and likewise for the downward direction. The average deposited energy is a subtraction of the two opposite-directed fluxes, and then the median is found from the resulting values as before. Again, voids have been excluded from the calculation as the inclusion of them would skew the results and have nonphysical values.

Where photoelectrons are the primary species ($90^\circ < \text{SZA} < 110^\circ$), the average energies of electrons are roughly 15–25 eV, characteristic energies of photoelectrons. Past $\text{SZA} = 110^\circ$, at higher elevation angles ($B_{\text{elev}} > 50^\circ$), the average upward energy is higher than the average downward energy, implying that

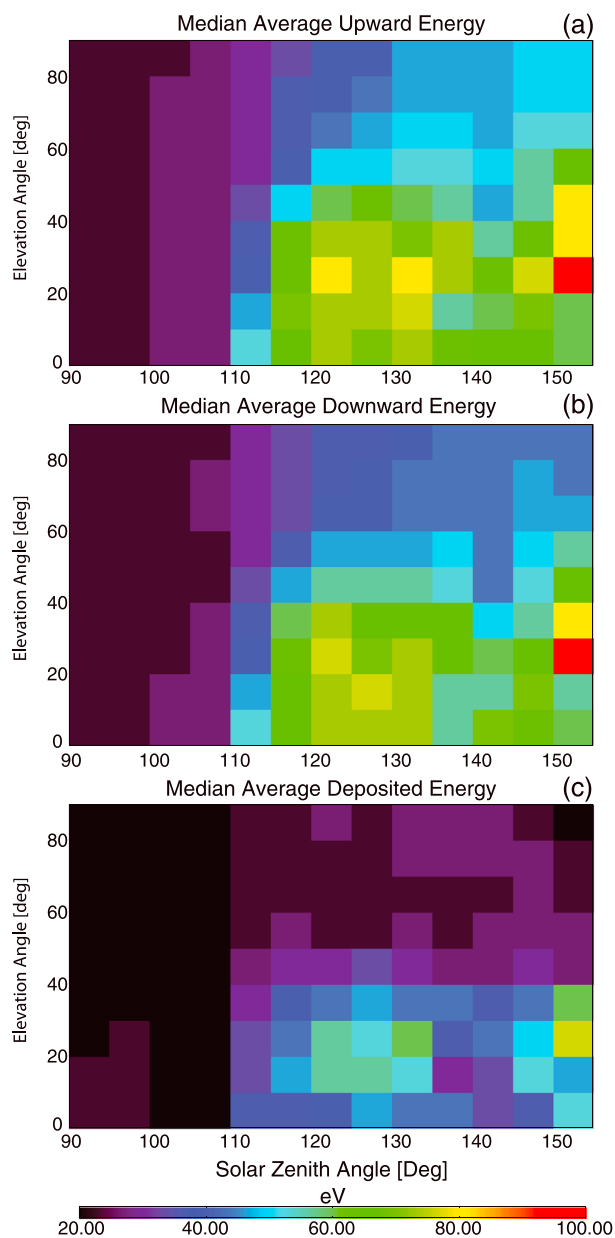


Figure 8. The median average energy for (a) upward directed electrons, (b) downward directed electrons, and (c) the deposited electrons. Voids are excluded in these calculations.

low-energy electrons are being deposited and higher-energy electrons are being magnetically reflected and/or scattered back out. The average energy for the deposited electrons is 20–30 eV, lower than the downward electrons in this region, affirming this conclusion. The average energy for all electrons is higher for lower elevation angles ($B_{\text{elev}} < 50^\circ$) than for greater elevation angles. High-energy trapped electrons are more likely to survive over lower energy trapped electrons.

The energy of the deposited electrons past the photoelectron source terminator is rather low, 20–30 eV. The depth of ionization due to these particles will occur around the photoelectron exobase, 140–180 km [e.g., Nagy and Banks, 1970; Lillis et al., 2008; Xu et al., 2016b]. They will not have the energy to penetrate deeper into the ionosphere, where Haider et al. [2007] found the peak ion layer to be ~130 km. The nightside ionosphere may have an ion peak shifted higher in altitude over areas where electrons are precipitating.

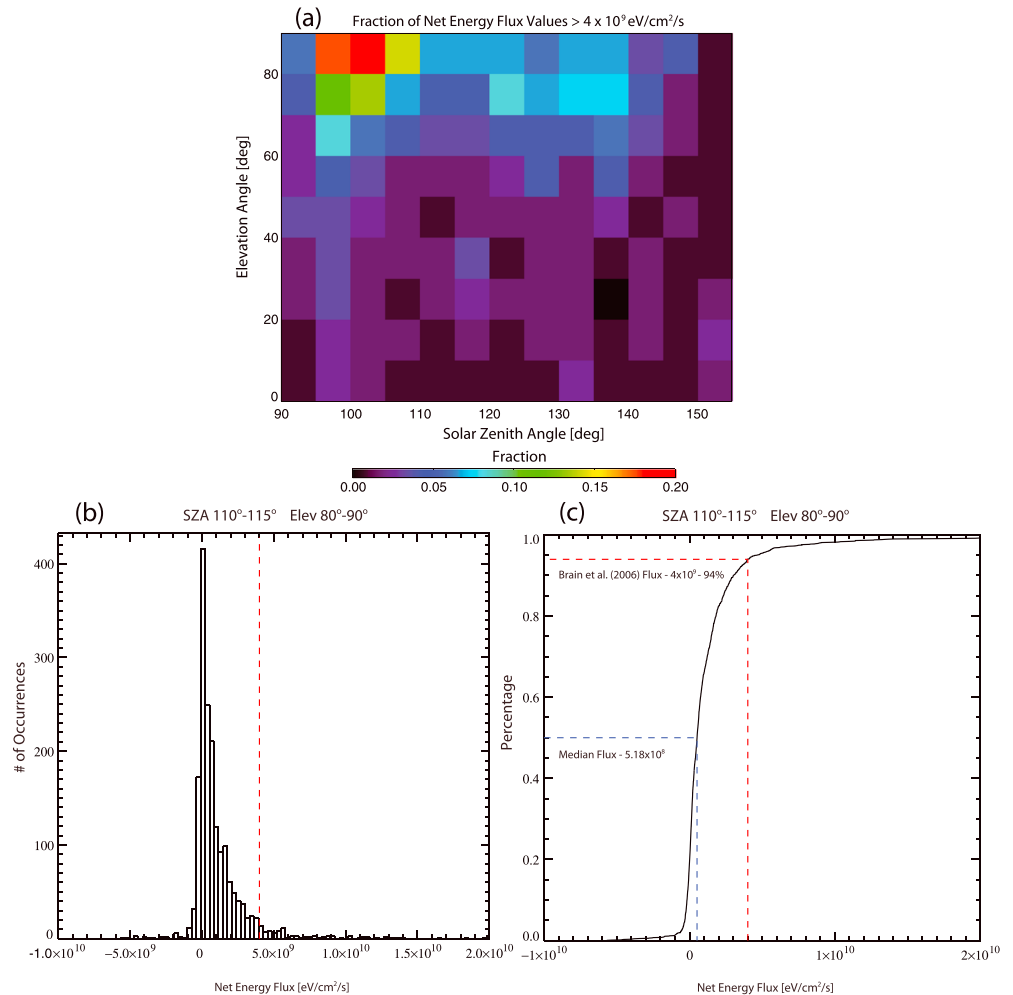


Figure 9. (a) The fraction of net energy flux values that exceed 4×10^9 eV/cm²/s. (b) Histogram of the net energy flux values for $SZA = 110^\circ - 115^\circ$ and $B_{\text{elev}} = 80^\circ - 90^\circ$. (c) CDF of the distribution in Figure 9b. The red dashed line denotes the *Brain et al.* [2006] value, and the blue dashed line is the median net energy flux.

3.5. Consequences of Energy Deposition

3.5.1. Excitation (Aurora)

Brain et al. [2006] investigated the possibility of aurora on Mars. They looked at peaked electron energy spectra and found peaks of 100 eV to 2.5 keV. They noted that many of the examined spectra, including the MEX event in *Bertaux et al.* [2005], occurred during solar energetic particle events. *Brain et al.* [2006] used a typical auroral-like energy spectra for analysis. The fluxes recorded were observed by MGS on 21 April 2001 over the strong crustal field region at $SZA \sim 125^\circ$. The downward flux at this time was 8.1×10^9 eV/cm²/s (1.3×10^{-2} mW/m²), and this flux was used as input to a model to estimate the amount of emission produced from the deposition of electrons. They note that half of this flux was deposited producing $\sim 4 R$ of emission from the CO₂⁺ (289.7 nm) line, which is ~ 17 times weaker than the MEX event.

Here we examined how many deposited energy flux occurrences in our analysis were greater than this deposited energy flux value of the *Brain et al.* [2006] study, 4×10^9 eV/cm²/s (6.4×10^{-3} mW/m²). The fraction of values that exceed this number is plotted in Figure 9a. We then looked specifically at the SZA/elevation angle bin that had the highest median net energy flux past 110°. This occurred at $SZA = 110^\circ - 115^\circ$ and at $B_{\text{elev}} = 80^\circ - 90^\circ$. Figures 9b and 9c show the histogram of net energy flux values in this bin and the cumulative distribution function (CDF), respectively. A red dashed line denotes the *Brain et al.* [2006] deposited energy flux value. The blue dashed line in Figure 9c is the median flux for this bin. The deposited energy flux exceeded the *Brain et al.* [2006] value only 6% of the time for this bin, and throughout the nightside along near-vertical field lines, it varies from 1 to 7%. There are values that reach up to 20%, but these are before the

photoelectron production terminator where the ionosphere is still sunlit. The energy flux needed to cause substantial emission does not occur all that often on the nightside.

3.5.2. Ionization

The creation of the nightside ionosphere of Mars is caused by day-to-night transport of electrons, precipitating electrons, or a combination thereof. Electron density profiles have been analyzed using radio occultations and predicted using models [e.g., *Fillingim et al.*, 2007; *Zhang et al.*, 2015, Table 1], and estimates of the peak density are on the order of 10^3 – 10^4 cm^{-3} . The average deposited flux in Figure 6f above SZA of 110° along near-vertical field lines is 2.0×10^8 $\text{eV}/\text{cm}^2/\text{s}$. We can divide this energy flux by the average energy to ionize a particle at Earth, 35 eV, and divide by the depth of the ionosphere, ~ 200 km [*Schunk and Nagy*, 2000]. This calculation produces a volume production rate of electrons of ~ 0.3 $\text{cm}^{-3} \text{s}^{-1}$. The collisional ionization cross section for CO_2 peaks at roughly 100 eV [*Strickland and Green*, 1969], however, so the ionization may be inefficient, due to the average energy of deposited electrons being 20–30 eV, and the presumed average ionization energy, 35 eV, may not be high enough. Therefore, the volume production rate is an upper bound for the flux value used.

With this production rate, the average density in the ionosphere can be estimated by

$$0.3 \text{ cm}^{-3} \text{ s}^{-1} = (n_{\text{O}_2^+})(n_{e^-})k \quad (1)$$

where $k = 6.4 \times 10^{-8} \text{ cm}^3 \text{ s}^{-1}$ [*Peveall et al.*, 2001], which is the dissociative recombination rate for O_2^+ , the most common ion in the ionosphere [e.g., *Hanson et al.*, 1977], when $T_e \sim 2000$ K. If we assume that the densities of O_2^+ and e^- are equal, i.e., photochemical equilibrium, then the average density produced by a net energy flux of 2.0×10^8 $\text{eV}/\text{cm}^2/\text{s}$ is $2.1 \times 10^3 \text{ cm}^{-3}$. Note that this calculation only accounts for near-vertical field lines over the strong crustal field region in the southern hemisphere.

However, we assumed a uniform electron distribution in a 200 km thick ionosphere, and our density value is an average throughout. A calculation of the total electron content (TEC) would be a better way to define this ionosphere. TEC values have been estimated at Mars [e.g., *Safaenili et al.*, 2007; *Lillis et al.*, 2009], and nightside values are on the order of 10^{14} m^{-2} [*Lillis et al.*, 2010, Figure 1a]. An average density of $2.1 \times 10^3 \text{ cm}^{-3}$ over 200 km corresponds to a TEC of $4.2 \times 10^{14} \text{ m}^{-2}$, which is agreeable with previous estimates.

Using a simple triangle distribution, a peak density can be calculated using $\text{TEC} = 4.2 \times 10^{14} \text{ m}^{-2}$. A peak layer of 160 km is used [e.g., *Fillingim et al.*, 2007], and this produces a peak density of $4.2 \times 10^3 \text{ cm}^{-3}$. *Fillingim et al.* [2007] used a model to do this same calculation, and our TEC calculations and maximum electron density calculations are on the same order of magnitude. In this study, pitch angle averaged net energy flux was used, while *Fillingim et al.* [2007] used differential downward energy flux. Our assumption of the average energy to ionize a particle is probably low, but these are quick calculations to understand the ionosphere our deposited flux values may cause. These values may be enough to support the nightside ionosphere in some areas, but other mechanisms such as day-to-night transport may be needed in other regions to sustain the ionosphere.

4. Conclusion

The same method utilized by *Xu et al.* [2014b] was used to classify the populations of photoelectrons and solar wind electrons and investigate superthermal electron energy deposition as measured by MGS on the nightside of Mars over the strong crustal field region. The ratio of two energy flux values at 47 eV and 115 eV will be greater for photoelectrons because of the knee in the energy spectra around 60–70 eV. Histograms as a function of solar zenith angle show a single-population distribution at low solar zenith angles ($\text{SZA} \leq 100^\circ$) centered around a flux ratio of 30. The distribution becomes bimodal with another peak around a flux ratio of 10 from $\text{SZA} = 100^\circ$ – 110° , and at $\text{SZA} = 110^\circ$, the histogram changes back into a single-population distribution losing the higher flux ratio peak. This demonstrates the photoelectron population being the dominant population while still in sunlit areas and eventually degrading in energy below instrument detection with increasing solar zenith angle leaving only solar wind electrons.

The occurrence rate was calculated as functions of solar zenith angle, elevation angle, and pitch angle. Voids are prominent at $\text{SZA} > 110^\circ$, past the photoelectron source terminator and away from magnetic loops with a sunlit foot point. This also is the solar zenith angle where the photoelectron population has sufficiently degraded. In the sunlit sectors, photoelectrons are the main population over all pitch angles and elevation angles. Once past the terminator, the field-aligned pitch angles are the first to lose their photoelectron

population. The perpendicular pitch angles are trapped thus having a longer lifespan. The occurrence rate then drops for horizontal elevation angles. These field structures tend to be shorter, and photoelectrons degrade in energy more quickly. The solar wind occurrence rate is highest at near-vertical field lines, more easily connected to the IMF.

The energy deposition on the nightside occurs primarily on vertical field lines and before the terminator on horizontal field lines. Typical nightside values for pitch angle averaged deposited flux are $\sim 2.0 \times 10^8$ eV/cm²/s. Past SZA = 110°, it is safe to assume that all energy deposition is due to solar wind electrons since histograms and occurrence rates show photoelectrons to be depleted by this point, especially from a statistical point of view. Note that this study used only MGS mapping phase data, at 2 A.M. local time, and so this cutoff is specific to that orbital constraint. The region on the nightside just past the terminator also has high flux values most likely due to a magnetic loop with one footprint on the dayside and the other on the nightside. More research into these regions could help answer questions about electron transport to the nightside and are probable regions for aurora. The maximum median fractional deposition rate found was 0.16. Most of the precipitating electrons are magnetically reflected or scattered back out. The average energy of deposited electrons was found to be 20–30 eV, perhaps creating an ion peak shifted upward in altitude in areas where electrons are precipitating on the nightside.

One consequence of electron deposition is excitation and emission. *Brain et al.* [2006] used a model and found that a deposited energy flux of 4×10^9 eV/cm²/s (6.4×10^{-3} mW/m²) will create $\sim 4 R$ of emission from CO₂⁺ (289.7 nm). We found that deposited electron energy flux values that exceed the *Brain et al.* [2006] value occur 1 to 7% of the time along near-vertical field lines.

Another consequence of electron deposition is ionization. Estimates of the TEC and peak density were calculated using an average deposited electron energy flux found in this study, 2.0×10^8 eV/cm²/s. The TEC was found to be 4.2×10^{14} m⁻² with a corresponding peak density of 4.2×10^3 cm⁻³. We note that this is limited to near-vertical field lines over the strong crustal field region past SZA of 110°.

It should be noted that the probabilities calculated in this study are based on a lower limit of the counts that is linked to the ER instrumental background threshold. There certainly could be photoelectron or solar wind electron fluxes below this limit that are neglected in the statistics presented above. Therefore, all of the probabilities for these two populations are lower limits, and the “void” probabilities are upper limits. That said, these neglected components of the electron populations are, by definition, at very low fluxes and are therefore not likely to cause an appreciable level of ionization or excitation in the thermosphere.

There is still further research to do from this study. A calculation of the decay rate of photoelectrons as a function of time in darkness and not solar zenith angle has not been done. This could be done through data analysis and compared to model results. A superthermal electron transport model has been developed for Mars [*Liemohn et al.*, 2003, 2006; *Xu and Liemohn*, 2015] and could be employed to ascertain the decay rate for photoelectrons.

Acknowledgments

The authors thank NASA for supporting this work, particularly under grants NNX13AF26G and NNX11AD80G. Most of MGS MAG/ER data are archived in the Planetary Data System (PDS), and the full MGS MAG/ER data set used in the paper is available upon request to David Mitchell (mitchell@ssl.berkeley.edu).

References

- Acuña, M. H., et al. (1998), Magnetic field and plasma observations at Mars: Initial results of the Mars Global Surveyor mission, *Science*, 279(5357), 1676–1680, doi:10.2307/2894341.
- Acuña, M. H., et al. (2001), Magnetic field of Mars: Summary of results from the aerobraking and mapping orbits, *J. Geophys. Res.*, 106(E10), 23,403–23,417, doi:10.1029/2000JE001404.
- Ashour-Abdalla, M., and C. F. Kennel (1978), Diffuse auroral precipitation, *J. Geomagn. Geoelectr.*, 30(3), 239–255, doi:10.5636/jgg.30.239.
- Banks, P. M., C. R. Chappell, and A. F. Nagy (1974), A new model for the interaction of auroral electrons with the atmosphere: Spectral degradation, backscatter, optical emission, and ionization, *J. Geophys. Res.*, 79(10), 1459–1470, doi:10.1029/JA079i010p01459.
- Bertaux, J.-L., F. Leblanc, O. Witasse, E. Quemerais, J. Liliensten, S. A. Stern, B. Sandel, and O. Korabely (2005), Discovery of an aurora on Mars, *Nature*, 435(7043), 790–794, doi:10.1038/nature03603.
- Brain, D., J. Halekas, R. Lillis, D. Mitchell, R. Lin, and D. Crider (2005), Variability of the altitude of the Martian sheath, *Geophys. Res. Lett.*, 32(18), L18203, doi:10.1029/2005GL023126.
- Brain, D. A., J. S. Halekas, L. M. Peticolas, R. P. Lin, J. G. Luhmann, D. L. Mitchell, G. T. Delory, S. W. Bougher, M. H. Acuña, and H. Rème (2006), On the origin of aurorae on Mars, *Geophys. Res. Lett.*, 33, L01201, doi:10.1029/2005GL024782.
- Brain, D. A., R. J. Lillis, D. L. Mitchell, J. S. Halekas, and R. P. Lin (2007), Electron pitch angle distributions as indicators of magnetic field topology near Mars, *J. Geophys. Res.*, 112, A09201, doi:10.1029/2007JA012435.
- Connerney, J. E. P., M. H. Acuña, P. J. Wasilewski, G. Kleteschka, N. F. Ness, H. Rème, R. P. Lin, and D. L. Mitchell (2001), The global magnetic field of Mars and implications for crustal evolution, *Geophys. Res. Lett.*, 28(21), 4015–4018, doi:10.1029/2001GL013619.
- Dubinin, E., M. Fraenz, J. Woch, J. Winningham, R. Frahm, R. Lundin, and S. Barabash (2008a), Suprathermal electron fluxes on the nightside of Mars: Aspera-3 observations, *Planet. Space Sci.*, 56(6), 846–851, doi:10.1016/j.pss.2007.12.010.

- Fillingim, M. O., L. M. Peticolas, R. J. Lillis, D. A. Brain, J. S. Halekas, D. L. Mitchell, R. P. Lin, D. Lummerzheim, S. W. Bougher, and D. L. Kirchner (2007), Model calculations of electron precipitation induced ionization patches on the nightside of Mars, *Geophys. Res. Lett.*, *34*, L12101, doi:10.1029/2007GL029986.
- Fillingim, M. O., L. M. Peticolas, R. J. Lillis, D. A. Brain, J. S. Halekas, D. Lummerzheim, and S. W. Bougher (2010), Localized ionization patches in the nighttime ionosphere of Mars and their electrodynamic consequences, *Icarus*, *206*(1), 112–119, doi:10.1016/j.icarus.2009.03.005.
- Fox, J. L., and A. I. F. Stewart (1991), The Venus ultraviolet aurora: A soft electron source, *J. Geophys. Res.*, *96*(A6), 9821–9828, doi:10.1029/91JA00252.
- Fox, J. L., J. F. Brannon, and H. S. Porter (1993), Upper limits to the nightside ionosphere of Mars, *Geophys. Res. Lett.*, *20*(13), 1339–1342, doi:10.1029/93GL01349.
- Gérard, J.-C., L. Soret, L. Libert, R. Lundin, A. Stiepen, A. Radioti, and J.-L. Bertaux (2015), Concurrent observations of ultraviolet aurora and energetic electron precipitation with Mars Express, *J. Geophys. Res. Space Physics*, *120*, 6749–6765, doi:10.1002/2015JA021150.
- Haider, S. A., J. Kim, A. F. Nagy, C. N. Keller, M. I. Verigin, K. I. Gringauz, N. M. Shutte, K. Szego, and P. Kiraly (1992), Calculated ionization rates, ion densities, and airglow emission rates due to precipitating electrons in the nightside ionosphere of Mars, *J. Geophys. Res.*, *97*(A7), 10,637–10,641, doi:10.1029/92JA00317.
- Haider, S. A., V. Singh, V. R. Choksi, W. C. Maguire, and M. I. Verigin (2007), Calculated densities of H_3O^+ (H_2O)_n, NO_2^- (H_2O)_n, CO_3^- (H_2O)_n and electron in the nighttime ionosphere of Mars: Impact of solar wind electron and galactic cosmic rays, *J. Geophys. Res.*, *112*, A12309, doi:10.1029/2007JA012530.
- Hanson, W. B., S. Sanatani, and D. R. Zuccaro (1977), The Martian ionosphere as observed by the Viking retarding potential analyzers, *J. Geophys. Res.*, *82*(28), 4351–4363, doi:10.1029/J5082i028p04351.
- Keating, G. M., S. W. Bougher, M. E. Theriot, R. H. Tolson, R. W. Zurek, R. C. Blanchard, J. R. Murphy, and J.-L. Bertaux (2007), Mars neutral upper atmosphere temporal and spatial variations discovered from the accelerometer science experiment aboard Mars Reconnaissance Orbiter, in *Lunar and Planetary Institute Conference Abstracts*, vol. 38, pp. 2074.
- Leblanc, F., J. Y. Chaufray, J. Liliensten, O. Witasse, and J.-L. Bertaux (2006), Martian dayglow as seen by the SPICAM UV spectrograph on Mars Express, *J. Geophys. Res.*, *111*, E09511, doi:10.1029/2005JE002664.
- Leblanc, F., et al. (2008), Observations of aurorae by SPICAM ultraviolet spectrograph on board Mars Express: Simultaneous ASPERA-3 and MARSIS measurements, *J. Geophys. Res.*, *113*, A08311, doi:10.1029/2008JA013033.
- Liemohn, M. W., G. V. Khazanov, T. E. Moore, and S. M. Guiter (1997), Self-consistent superthermal electron effects on plasmaspheric refilling, *J. Geophys. Res.*, *102*(A4), 7523–7536, doi:10.1029/96JA03962.
- Liemohn, M. W., D. L. Mitchell, A. F. Nagy, J. L. Fox, T. W. Reimer, and Y. Ma (2003), Comparisons of electron fluxes measured in the crustal fields at Mars by the MGS Magnetometer/Electron Reflectometer instrument with a *B* field-dependent transport code, *J. Geophys. Res.*, *108*(E12), 5134, doi:10.1029/2003JE002158.
- Liemohn, M. W., R. A. Frahm, J. D. Winningham, Y. Ma, S. Barabash, R. Lundin, and J. U. Kozyra (2006), Numerical interpretation of high-altitude photoelectron observations, *Icarus*, *182*(2), 383–395, doi:10.1016/j.icarus.2005.10.036.
- Liemohn, M. W., Y. Ma, A. F. Nagy, J. U. Kozyra, J. D. Winningham, R. A. Frahm, J. S. Sharber, S. Barabash, and R. Lundin (2007), Numerical modeling of the magnetic topology near Mars auroral observations, *Geophys. Res. Lett.*, *34*, L24202, doi:10.1029/2007GL031806.
- Lillis, R. J., and D. A. Brain (2013), Nightside electron precipitation at Mars: Geographic variability and dependence on solar wind conditions, *J. Geophys. Res. Space Physics*, *118*, 3546–3556, doi:10.1002/jgra50171.
- Lillis, R. J., D. L. Mitchell, R. P. Lin, and M. H. Acuña (2008), Electron reflectometry in the Martian atmosphere, *Icarus*, *194*, 544–561, doi:10.1016/j.icarus.2007.09.030.
- Lillis, R. J., M. O. Fillingim, L. M. Peticolas, D. A. Brain, R. P. Lin, and S. W. Bougher (2009), Nightside ionosphere of Mars: Modeling the effects of crustal magnetic fields and electron pitch angle distributions on electron impact ionization, *J. Geophys. Res.*, *114*, E11009, doi:10.1029/2009JE003379.
- Lillis, R. J., D. A. Brain, S. L. England, P. Withers, M. O. Fillingim, and A. Safaeinili (2010), Total electron content in the Mars ionosphere: Temporal studies and dependence on solar EUV flux, *J. Geophys. Res.*, *115*, A11314, doi:10.1029/2010JA015698.
- Lundin, R., D. Winningham, S. Barabash, R. A. Frahm, H. Andersson, M. Holmstrom, and A. Grigoriev (2006a), Ionospheric plasma acceleration at Mars: ASPERA-3 results, *Icarus*, *182*(2), 308–319, doi:10.1016/j.icarus.2005.10.035.
- Lundin, R., et al. (2006b), Plasma acceleration above Martian magnetic anomalies, *Science*, *311*(5763), 980–983, doi:10.2307/3843558.
- Mantas, G. P., and W. B. Hanson (1979), Photoelectron fluxes in the Martian ionosphere, *J. Geophys. Res.*, *84*(A2), 369–385, doi:10.1029/JA084iA02p00369.
- Mitchell, D. L., R. P. Lin, C. Mazelle, H. Rème, P. A. Cloutier, J. E. P. Connerney, M. H. Acuña, and N. F. Ness (2001), Probing Mars' crustal magnetic field and ionosphere with the MGS Electron Reflectometer, *J. Geophys. Res.*, *106*(E10), 23,419–23,427, doi:10.1029/2000JE001435.
- Nagy, A. F., and P. M. Banks (1970), Photoelectron fluxes in the ionosphere, *J. Geophys. Res.*, *75*(31), 6260–6270, doi:10.1029/JA075i031p06260.
- Nagy, A., et al. (2004), The plasma environment of Mars, in *Mars Magnetism and Its Interaction With the Solar Wind*, edited by D. Winterhalter, M. Acuña, and A. Zakharov, pp. 33–114, Springer, Netherlands.
- Němec, F., D. D. Morgan, D. A. Gurnett, and F. Duru (2010), Nightside ionosphere of Mars: Radar soundings by the Mars Express spacecraft, *J. Geophys. Res.*, *115*, E12009, doi:10.1029/2010JE003663.
- Němec, F., D. D. Morgan, D. A. Gurnett, and D. A. Brain (2011), Areas of enhanced ionization in the deep nightside ionosphere of Mars, *J. Geophys. Res.*, *116*, E06006, doi:10.1029/2011JE003804.
- Peverall, R., et al. (2001), Dissociative recombination and excitation of O_2^+ : Cross sections, product yields and implications for studies of ionospheric airglows, *J. Chem. Phys.*, *114*(15), 6679–6689, doi:10.1063/1.1349079.
- Safaeinili, A., W. Kofman, J. Mougnot, Y. Gim, A. Herique, A. B. Ivanov, J. J. Plaut, and G. Picardi (2007), Estimation of the total electron content of the Martian ionosphere using radar sounder surface echoes, *Geophys. Res. Lett.*, *34*, L23204, doi:10.1029/2007GL032154.
- Schunk, R., and A. Nagy (2000), *Ionospheres: Physics, Plasma Physics, and Chemistry*, Cambridge Atmos. and Space Sci. Ser., vol. 59, Cambridge Univ. Press, New York.
- Soret, L., J.-C. Gérard, L. Libert, V. I. Shematovich, D. V. Bisikalo, A. Stiepen, and J.-L. Bertaux (2015), SPICAM observations and modeling of Mars aurorae, *Icarus*, *264*, 398–406, doi:10.1016/j.icarus.2015.09.023.
- Steckiewicz, M., et al. (2015), Altitude dependence of nightside Martian suprathermal electron depletions as revealed by MAVEN observations, *Geophys. Res. Lett.*, *42*, 8877–8884, doi:10.1002/2015GL065257.

- Strickland, D. J., and A. E. S. Green (1969), Electron impact cross sections for CO₂, *J. Geophys. Res.*, *74*(26), 6415–6424, doi:10.1029/JA074i026p06415.
- Swift, D. W. (1981), Mechanisms for auroral precipitation: A review, *Rev. Geophys.*, *19*(1), 185–211, doi:10.1029/RG019i001p00185.
- Verigin, M. I., K. I. Gringauz, N. M. Shutte, S. A. Haider, K. Szego, P. Kiraly, A. F. Nagy, and T. I. Gombosi (1991), On the possible source of the ionization in the nighttime Martian ionosphere: 1. Phobos 2 HARP electron spectrometer measurements, *J. Geophys. Res.*, *96*(A11), 19,307–19,313, doi:10.1029/91JA00924.
- Xu, S., and M. W. Liemohn (2015), Superthermal electron transport model for Mars, *Earth Space Sci.*, *2*(3), 47–64, doi:10.1002/2014EA000043.
- Xu, S., M. W. Liemohn, D. L. Mitchell, and M. D. Smith (2014a), Mars photoelectron energy and pitch angle dependence on intense lower atmospheric dust storms, *J. Geophys. Res. Planets*, *119*, 1689–1706, doi:10.1002/2013JE004594.
- Xu, S., M. W. Liemohn, and D. L. Mitchell (2014b), Solar wind electron precipitation into the dayside Martian upper atmosphere through the cusps of strong crustal fields, *J. Geophys. Res. Space Physics*, *119*, 10,100–10,115, doi:10.1002/2014JA020363.
- Xu, S., M. W. Liemohn, S. Bougher, and D. L. Mitchell (2016a), Enhanced carbon dioxide causing the dust storm-related increase in high-altitude photoelectron fluxes at Mars, *Geophys. Res. Lett.*, *42*, 9702–9710, doi:10.1002/2015GL066043.
- Xu, S., M. Liemohn, S. Bougher, and D. Mitchell (2016b), Martian high-altitude photoelectrons independent of solar zenith angle, *J. Geophys. Res. Space Physics*, *121*, doi:10.1002/2015JA022149.
- Zhang, S., J. Cui, P. Guo, J. L. Li, J. S. Ping, N. C. Jian, and K. F. Zhang (2015), Martian electron density profiles retrieved from Mars Express dual-frequency radio occultation measurements, *Adv. Space Res.*, *55*(9), 2177–2189, doi:10.1016/j.asr.2015.01.030.